

Anomalous photoluminescence enhancement and resonance charge transfer in type-II 2D lateral heterostructures

Chun-Yan Zhao(赵春艳), Sha-Sha Li(李莎莎), and Yong Yan(闫勇)

Citation: Chin. Phys. B, 2023, 32 (**8**): 087801. DOI: 10.1088/1674-1056/acc1d1
Journal homepage: http://cpb.iphy.ac.cn; http://iopscience.iop.org/cpb

What follows is a list of articles you may be interested in

Enhanced absorption process in the thin active region of GaAs based p-i-n structure

Chen Yue(岳琛), Xian-Sheng Tang(唐先胜), Yang-Feng Li(李阳锋), Wen-Qi Wang(王文奇), Xin-Xin Li(李欣欣), Jun-Yang Zhang(张珺玚), Zhen Deng(邓震), Chun-Hua Du(杜春花), Hai-Qiang Jia(贾海强), Wen-Xin Wang(王文新), Wei Lu(陆卫), Yang Jiang(江洋), and Hong Chen(陈弘)

Chin. Phys. B, 2021, 30 (**9**): 097803. DOI: 10.1088/1674-1056/abf10c

Low-dimensional phases engineering for improving the emission efficiency and stability of quasi-2D perovskite films

Yue Wang(王月), Zhuang-Zhuang Ma(马壮壮), Ying Li(李营), Fei Zhang(张飞), Xu Chen(陈旭), and Zhi-Feng Shi(史志锋)

Chin. Phys. B, 2021, 30 (**6**): 067802. DOI: 10.1088/1674-1056/abe92b

Thermally induced band hybridization in bilayer-bilayer MoS_2/WS_2 heterostructure

Yanchong Zhao(赵岩翀), Tao Bo(薄涛), Luojun Du(杜罗军), Jinpeng Tian(田金朋), Xiaomei Li(李晓梅), Kenji Watanabe, Takashi Taniguchi, Rong Yang(杨蓉), Dongxia Shi(时东霞), Sheng Meng(孟胜), Wei Yang(杨威), and Guangyu Zhang(张广宇)

Chin. Phys. B, 2021, 30 (**5**): 057801. DOI: 10.1088/1674-1056/abeee3

Effect of Sb composition on the band alignment of InAs/GaAsSb quantum dots

Guangze Lu(陆光泽), Zunren Lv(吕尊仁), Zhongkai Zhang(张中恺), Xiaoguang Yang(杨晓光), and Tao Yang(杨涛)

Chin. Phys. B, 2021, 30 (**1**): 017802. DOI: 10.1088/1674-1056/abb309

Surface plasmon enhanced photoluminescence in amorphous silicon carbide films by adjusting Ag island film sizes

Yu Wei (于威), Wang Xin-Zhan (王新占), Dai Wan-Lei (戴万雷), Lu Wan-Bing (路万兵), Liu Yu-Mei (刘玉梅), Fu Guang-Sheng (傅广生)

Chin. Phys. B, 2013, 22 (**5**): 057804. DOI: 10.1088/1674-1056/22/5/057804

Anomalous photoluminescence enhancement and resonance charge transfer in type-II 2D lateral heterostructures

Chun-Yan Zhao(赵春艳)[1], Sha-Sha Li(李莎莎)[2], and Yong Yan(闫勇)[1,†]

[1] *School of Physics, Henan Key Laboratory of Photovoltaic Materials, Henan Normal University, Xinxiang* 453007, *China*
[2] *School of Electronic Engineering, Chaohu University, Hefei* 238024, *China*

(Received 5 November 2022; revised manuscript received 26 February 2023; accepted manuscript online 7 March 2023)

Type-II band alignment can realize the efficient charge transfer and separation at the semiconductor heterointerface, which results in photoluminescence (PL) quenching. Recently, several researches demonstrated great enhancement of localized PL at the interface of type-II two-dimensional (2D) heterostructure. However, the dominant physical mechanism of this enhanced PL emission has not been well understood. In this work, we symmetrically study the exciton dynamics of type-II lateral heterostructures of monolayer MoS_2 and WS_2 at room temperatures. The strong PL enhancement along the one-dimensional (1D) heterointerface is associated with the trion emission of the WS_2 shell, while a dramatic PL quenching of neutral exciton is observed on the MoS_2 core. The enhanced quantum yield of WS_2 trion emission can be explained by charge-transfer-enhanced photoexcited carrier dynamics, which is facilitated by resonance hole transfer from MoS_2 side to WS_2 side. This work sheds light on the 1D exciton photophysics in lateral heterostructures, which has the potential to lead to new concepts and applications of optoelectronic device.

Keywords: lateral heterostructures, resonance charge transfer, MoS_2/WS_2, photoluminescence enhancement, band alignment.

PACS: 78.66.Li, 78.40.Fy, 68.47.Fg, 68.35.bg **DOI:** 10.1088/1674-1056/acc1d1

1. Introduction

Two-dimensional (2D) transition metal dichalcogenides (TMDCs), such as MoS_2, WS_2, $MoSe_2$, and WSe_2, have potential applications in ultrathin electronics and optics because they exhibit distinctive electro-optical properties.[1–5] Unlike their bulk form, all these monolayer TMDCs are direct bandgap semiconductors that feature strong light-matter coupling and considerably strengthened electron–electron/electron–phonon interactions as compared with conventional semiconductors such as silicon or germanium.[6] Different monolayer TMDCs can be combined within an atomically thin optoelectronic device and form vertical or lateral heterostructures (HSs). As each component has a different electronic structure and physical properties, HSs have shown fascinating features by taking advantage of the synergy effect, for example, the hot carrier photovoltaic cells,[7] steep slope tunnel transistors,[8] and the formation of long-lived interlayer excitons.[9]

Lateral heterostructure (LHS) refers to a material system that consists of different 2D monolayer crystals bonded in one plane. The LHS with three types of energy band alignments is a key component for constructing monolayer rectifying diode, electroluminescent device, and quantum device.[10,11] Especially, the staggered (type-II) band alignment will drive an efficient charge transfer of photogenerated carriers, so that the electrons accumulate on one side and the holes swept by the build-in electrical field on the other side. Therefore, the type-II LHSs have promising applications in photovoltaic devices with fast charge separation and slow charge recombination,[12] which are responsible for the photoluminescence (PL) quenching.[13] Nevertheless, recently, a strong localized PL enhancement was observed at the interface of the MoS_2/WS_2 LHS with a typical type-II band alignment.[10] A clear photovoltaic effect, meanwhile, was observed in the same LHS under illumination, which is also solid evidence of the photogenerated carrier separation. It is confusing that radiative recombination of excitons and separation of charge carriers under the built-in electric field can occur simultaneously at the interface. The authors contributed the anomalous PL enhancement to the photogenerated electron–hole pairs preferential recombination in the vicinity of the interface that serves as an excitonic recombination center. This mechanism seems to be universal. Large PL enhancement in WS_2 flakes was excited by an out-of-plane magnetic field because of a larger overlap of the electron and hole caused by the magnetic field induced confinement.[14] Additionally, the substitution of lattice for oxygen clusters can also induce the dramatic PL enhancement of monolayer WS_2.[15] On the contrary, the other lateral TMDC HSs do not exhibit anomalous PL enhancement.[16–20] Consequently, there is a surprising lack of rational explanation about the origin for such an anomalous PL enhancement as well as about the detailed influence of charge transfer on the excitonic properties.

In this work, we propose a paradigm to explain the un-

[†]Corresponding author. E-mail: yanyong@htu.edu.cn

© 2023 Chinese Physical Society and IOP Publishing Ltd

derlying physical mechanism for the strong localized PL enhancement in the type-II MoS_2/WS_2 LHS. The steady-state PL microscopy demonstrates that the enhanced PL emission in the vicinity of the interface is dominated by negative-trion recombination of WS_2, meanwhile, normal PL quenching is observed on the MoS_2 side. The high enhancement of PL quantum efficiency of negative-trion can be explained by novel carrier dynamics, which is facilitated by resonance hole transfer from MoS_2 to WS_2 and alternate recombination channels in WS_2. This ultrafast hole redistribution at the interface on photoexcitation results from the energy level alignment of valance bands in MoS_2/WS_2 LHS, which is confirmed by first-principles calculations. This study provides novel insights into exciton photophysics in MoS_2/WS_2 LHSs.

2. Experiment

2.1. Growth of monolayer lateral HSs

The controllable synthesis of 2D MoS_2/WS_2 lateral HS *via* CVD growth is schematically illustrated in Figs. 1(a) and 1(b). The MoS_2/WS_2 lateral HS nanosheets were grown on the 300-nm SiO_2/Si substrates through a one-pot CVD method. The substrates were treated by using oxygen plasma for 20 s to transform its surface from weakly hydrophilic surface into hydrophilic surface. The MoO_3 and WO_3 powder were utilized as the Mo precursor and W precursor, respectively. The aqueous MoO_3 and WO_3 dispersions with different concentrations (2 mg/mL–10 mg/mL) were prepared by adding MoO_3 (Aladdin, 99.5%) and WO_3 powders (Sigma-Aldrich, 95%), respectively, into 5-mM NaCl deionized (DI) water solution. The MoO_3 dispersions with $\sim$ 30 μL were sonicated and stirred over 10 min and then distributed on a quartz boat. Subsequently, the quartz boat with dispersions was dried in the vacuum drying oven for 5 h. The WO_3 dispersions were coated in the inner wall of a quartz tube (OD: 12 cm, length: 5 cm). A piece of the substrate was placed into the quartz tube with the silica side facing to W source and then placed into the central temperature zone of the tube furnace as shown in Fig. 1(a). The distance between the Mo source and W source was about 4.5 cm. Sulfur powders were placed upstream in the tube. The synthesis of MoS_2/WS_2 lateral HSs was performed *via* introducing 50-sccm N_2 to grow MoS_2 at the first stage (720 °C, 3 min). The S powder was heated to 200 °C for 1 min after the center of the quartz tube had risen to 700 °C. And then, the furnace was maintained at 860 °C for 5 min as the second stage to grow MoS_2/WS_2 lateral HSs.

2.2. Optical property characterization

Optical images of MoS_2/WS_2 LHSs were obtained on an optical microscope (Zeiss Axio Scope A1). Raman spectra and mapping were achieved *via* a confocal laser microscope system (Alpha 300RA, WITec). Micro photoluminescence (PL) spectra and mapping were performed on Renishaw inVia micro-Raman spectroscope (532-nm laser). The integrated time for each spectrum was set to be 10 s and the laser power was set to be 2 μW. The kinetics of the ultrafast photophysical interactions were performed by transient absorption microscopy with reflection mode. Each region was excited by a 400-nm laser (with a laser spot size of $\sim$ 4 μm) generated by an 800-nm ultrashort pulse laser with a repetition rate of 80 MHz and a pulse duration of $\sim$ 120 fs. The probe beam was supercontinuum light generated by the same ultrashort pulse laser. Both the pump beam and probe beam were focused and spatially overlapped on the sample. The relative reference light ($\Delta R/R_0$) induced by the pump was recorded by using a detector.

2.3. Theoretical calculations

The electronic structure calculations were performed by using the density functional theory (DFT)-based first-principles methods, which are implemented in the Vienna *ab initio* simulation package (VASP).[21–24] The Perdew–Burke–Ernzerhof functional of the generalized gradient approximation was adopted to describe the exchange–correlation potential. Moreover, the projected augmented wave potential was used to model the electron–ion potential. All calculations were carried out for an 8×4×1 supercell with 16 Mo atoms, 16 W atoms, and 64 S atoms. The kinetic energy cutoff was set to be 500 eV and the vacuum level was assumed to be larger than 20 Å to avoid the interaction between the adjacent layers. And the structures were fully relaxed until the force on each atom was less than 0.01 eV/Å, the convergence criterion of total energy was chosen to be 10^{-6} eV.

3. Results and discussion

The 2D MoS_2/WS_2 LHSs are synthesized on Si/silicon oxide (300 nm in thickness) wafers *via* the one-pot chemical vapor deposition (CVD) method. Sample fabrication details are available in the supplementary materials. The as-grown MoS_2/WS_2 LHS is characterized by optical microscopy (OM), atomic force microscopy (AFM), and Raman microscopy. The MoS_2 and WS_2 present the typical triangular shape in Figs. 1(c) and 1(d), respectively. The MoS_2/WS_2 LHS with a core-shell nanostructure distributes randomly on the substrate as shown in Fig. 1(e). Atomic force microscopy (AFM) measurements are conducted to verify the thickness of the MoS_2/WS_2 LHS lateral heterostructure, and the results are shown in Fig. 1(f). The thickness across the heterojunction is approximately 1.04 nm, indicating its monolayer characteristics. Figure 2(a) shows the OM image of a typical MoS_2/WS_2 LHS, in which the 1D lateral interface between the MoS_2 core and the WS_2 shell is easily distinguished by the color contrast.

The domain size is much larger than the LHS size reported in previous researches.[25,26] Furthermore, Raman spectrum is utilized to identify the MoS_2 domain, the WS_2 domain, and the interface of MoS_2/WS_2 lateral HS. Figure 2(b) illustrates the Raman spectra acquired in three regions, respectively. The excitation source is a 532-nm laser (2.33 eV) with a laser spot size of approximately 0.5 μm and the power at the sample is estimated at below 10 mW. Raman spectrum collected from the central region demonstrates two characteristic peaks at 384 cm^{-1} (E^1_{2g}) and 403 cm^{-1} (A_{1g}) which is consistent with the reported monolayer MoS_2.[27] By comparisons, the in-plane E^2_{2g}, $2LA+E^1_{2g}$, and out-of-plane A_{1g} modes are observed at 325 cm^{-1}, 349 cm^{-1}, and 418 cm^{-1} in the spectrum taken from the marginal WS_2 region, respectively.[28] The Raman spectrum obtained from the interface HS region shows the superposition of Raman shifts of MoS_2 and WS_2, suggesting the coexistence of these two materials. Raman intensity mappings at 384 cm^{-1} and 349 cm^{-1} further confirm the spatial distribution of MoS_2 region and WS_2 regions in the HS. Raman mapping shows a clear and sharp interface formed in the LHS, providing unique opportunities to study physical phenomena in the 1D limit. The area of the MoS_2 core is 1236 μm^2. The width and area of the WS_2 shell are about 11.2 μm and 2708 μm^2, respectively. The profile of the WS_2 shell exactly duplicates the shape of the MoS_2 core, confirming the lateral epitaxy of WS_2 on MoS_2 edges.

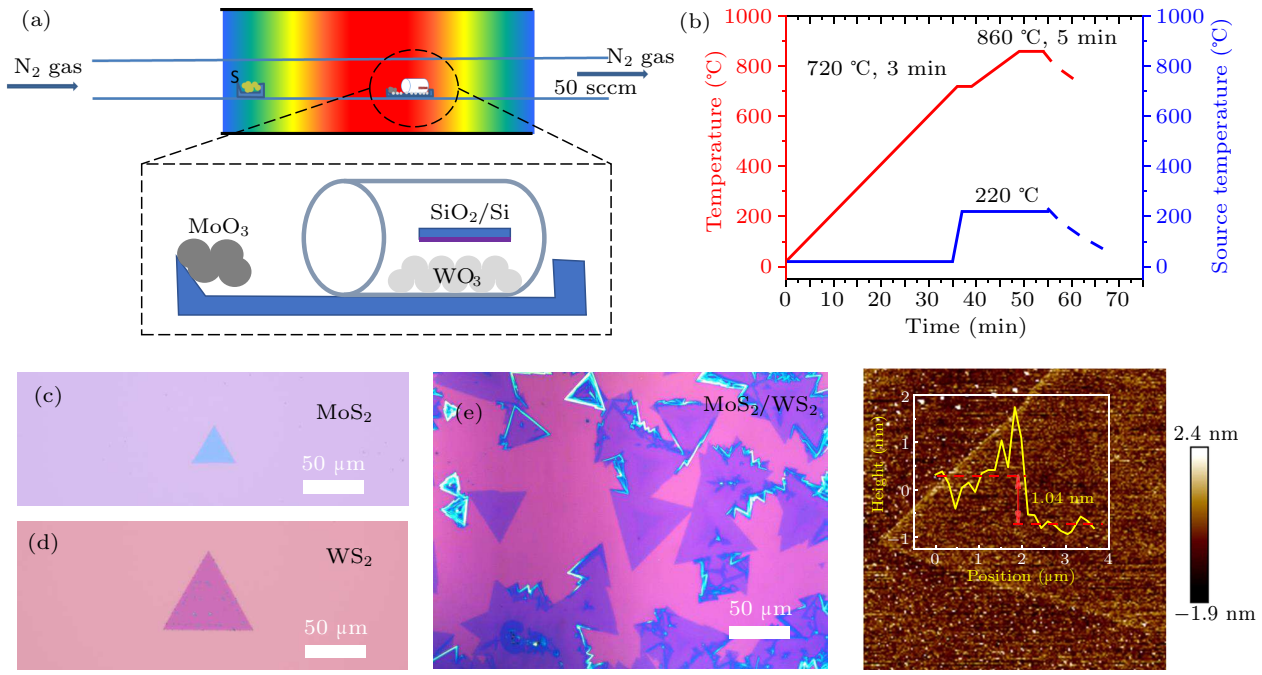


Fig. 1. Synthesis of 2D MoS_2/WS_2 LHS. (a) Schematic diagram of one-pot CVD approach. (b) Temperature evolutions of the reaction furnace. (c)–(e) Optical image of typical isolated MoS_2, WS_2, and MoS_2/WS_2 LHS prepared under different conditions. (f) AFM image of synthesized MoS_2/WS_2 LHS showing good single layer thickness uniformity.

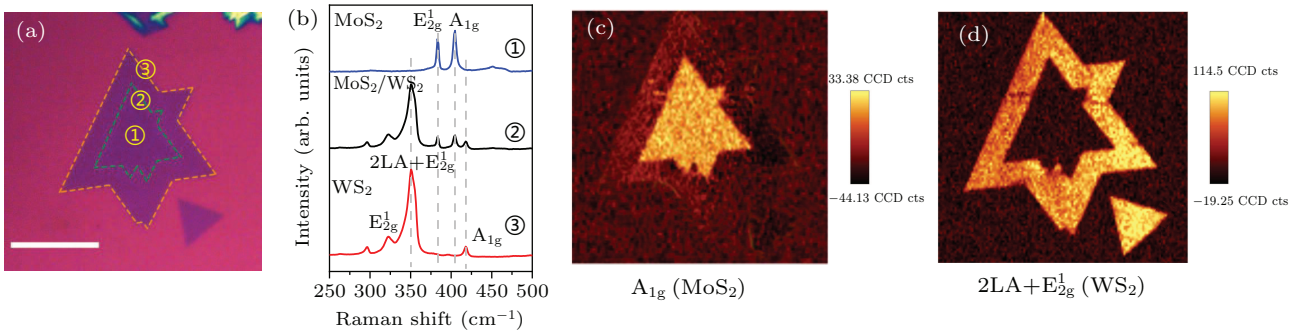


Fig. 2. (a) Optical microscope image of MoS_2/WS_2 LHS, with e scale bar being 50 μm. (b) Raman spectrum of MoS_2 core, MoS_2/WS_2 interface, and WS_2 shell, respectively. (c) and (d) Raman mapping of MoS_2/WS_2 LHS.

To identify the excitonic features, we measure the PL spectra of monolayer MoS_2/WS_2 LHS at room temperature. Figure 3 shows a high-resolution PL microscope image from the MoS_2/WS_2 LHS monolayer to assess the interfacial excitonic effect. The PL mapping confirms its unique core–shell structure. The PL spectrum (see Fig. S1 in supporting information) with a sharp peak located at around 669 nm (1.85 eV) is consistent with the direct excitonic transition en-

ergy in monolayer MoS_2 at room temperature. Moreover, the PL peak observed at 627 nm (1.98 eV) is contributed by the A^0 excitonic emission of the WS_2 shell, indicating its monolayer thickness.[28,29] The MoS_2 core (Fig. 3(b)) exhibits the uniform distribution of PL intensity, besides, the PL quenching region in the vicinity of the LHS interface. However, the WS_2 shell displays two extraordinarily bright emission regions at both edges and one weaker emission region in the middle. The spatial width of the WS_2 A^0 excitonic emission (9.8 μm) is less than the WS_2 shell width acquired from Raman mapping (11.2 μm). In other words, the inner highly localized PL enhancement region is clearly shown 1.4 μm away from the lateral interfaces (green dotted line), which is consistent with the scenario of half of the depletion width (2.2 μm).[30] In a one-step growth process, the formation of Mo vacancies may occur at the edge of MoS_2 core, since a small amount of MoO_3 dispersion is used to fabricate MoS_2 crystals. The effect of Mo vacancy is negligible in the conduction band but significant in the valence band with the occupied acceptor level near the valence band maximum,[31] resulting in lower electron concentration and wider dark depletion region at the edge of MoS_2 core.

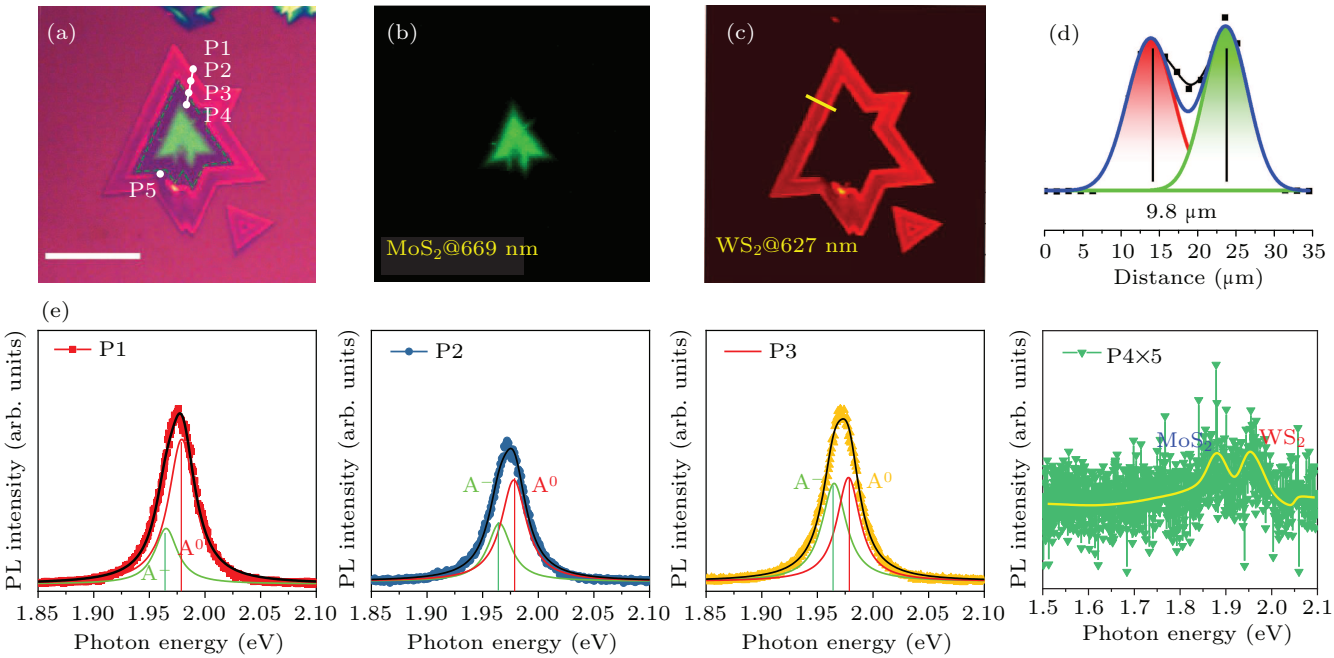


Fig. 3. PL intensity mapping of MoS_2/WS_2 LHS. (a) Integrated OM image and individual PL mapping of the same crystal, (b) MoS_2 distribution, and (c) WS_2 distribution. (d) Intensity profile of the yellow line in panel (c). (e) PL spectra of the marked regions in panel (a), fitted with two Gaussian peaks representing exciton (A^0) and negative trion (A^-) emission. The scale bar is 50 μm.

To clearly illustrate the evolutions of the spectra from the WS_2 shell, the PL spectra obtained at positions P1–P5 are shown in Fig. 3(d), respectively. The spectral weight of the peak changes with the position, *i.e.*, the relative proportion of the exciton peak decreases while that of trion peak increases. Generally, the PL enhancement at the edge of TMDC is considered to be a result of contributions from different kinds of quasiparticles, namely neutral exciton, negative/positive trions, and biexcitons.[29] Previous work on WS_2 monolayers has shown the edge enhancement and spatial non-uniformities of the PL spectrum.[28,32,33] The red curve obtained at P1 shows a relatively strong peak located at ∼ 1.98 eV with a full width at half-maximum (FWHM) value of 25.0 meV, corresponding to the neutral A^0 exciton emission.[28,29,34,35] The PL peak positions gradually change from 1.98 eV (P1) to 1.95 eV (P4) with the general decay of the PL peak intensities. The PL intensity from location P2 is weaker than that of the spectrum obtained from location P3. The variation of the spectral weight can be ascribed to the fact that the formation of negative trions (A^-) is energetically favorable at the interior edge.[33] The corresponding average photon energy for A^- in the WS_2 is ∼ 1.96 eV, in accordance with the previous result.[35] The PL spectrum at the location P2 shows weaker exciton emission and the trion emission almost remains unchanged. In contrast, the inner edge (P3) shows a stronger trion emission and the peak height of trion emission is comparable to that of neutral exciton emission. Additionally, the proportion of neutral exciton emission at P2 and at P3 are almost equal. In the interface region (P4), the exciton peak vanishes. For more clarity, the noted spectral feature in the PL spectrum is fitted with two peaks (A^0 and A^-); the peak positions, FWHM, and the area ratio of the A^0 emission to A^- emission are summarized in Table 1. We can find a slight redshift (∼ 10 meV) from P1 to P4, which may be attributed to the formation of laser-induced defective states near the band edge of WS_2.[15] With an investigation in detail, strong and highly localized PL enhancement

shows somewhat diminished at position P5. The corresponding PL spectrum (Fig. S2) is deconvoluted into three Gaussian peaks, which are assigned (from higher to lower energy) to the neutral A^0 exciton, negatively charged A^- exciton, and defect-bound exciton (D) emission from localized states.[32] The peak at 1.94 eV indicates that the excitons are bound to a shallow defect state since the defect-related exciton leads to lower emission energy. Therefore, the photophysical mechanism of the localized PL enhancement 1.5 μm away from the interface can be attributed to the enhanced recombination of negative A^- trions. A depletion region is formed at the MoS_2/WS_2 interface due to the type-II band alignment,[36] and the LHS allows more space to form the depletion region with a considerable built-in electric field.[30] Interfacial depletion region plays a key role in facilitating carrier separation and cannot act as an excitonic recombination center.[10] While, the underlying mechanism of A^- emission enhancement remains unknown. Next, we address this question and elucidate the nature of negative A^- trions.

Table 1. PL peak positions and FWHMs of typical MoS_2/WS_2 LHS.

Position	A^0 (eV)	A^- (eV)	Area ratio (A^0/A^-)	FWHM A^0 (meV)	FWHM A^- (meV)
P1	1.985	1.962	3.038	25.02	29.20
P2	1.982	1.960	1.890	25.41	28.31
P3	1.976	1.958	1.007	26.82	25.50
P4	–	1.952	–	–	50.24
P5	1.978	1.964	0.234	29.38	22.48

Charge transfer is an effective way to manipulate the exciton and trion quasiparticles in monolayer TMDCs.[37] The depletion region in type-II HS provides charge transfer under the build-in electric field, thus it is bound to affect the PL quantum yields.[38] We then perform transient absorption microscopy (TAM) to obtain solid evidence for the formation of a depletion region in the sample and further understand the enhanced trion PL emission in MoS_2/WS_2 LHS.

Figure 4(a) shows the mapping of TAM spectra as a function of pump–probe delay time for bare WS_2 shell. A distinct positive peak (photobleaching, PB) around 1.98 eV, corresponding to the ground-state bleaching of the A exciton peak of the WS_2 crystal, can be observed.[39] The PB peak shows a triple exponential decay feature, specifically, $y = A_1\exp(-x/\tau_1) + A_2\exp(-x/\tau_2) + A_3\exp(-x/\tau_3)$, with corresponding lifetimes $\tau_1 = 0.3$ ps, $\tau_2 = 4.7$ ps, and $\tau_3 = 38.2$ ps. The fast component τ_1 is generally believed to be caused by the charges trapped by surface-defect trap states.[40] The intermediate decay time constant (τ_2) is assigned to carrier–photon scattering.[41] The slowest decay component (τ_3) on the order of tens of picoseconds is related to a direct interband electron–hole recombination in WS_2. The negative peaks around the A exciton peak originates from broad photoinduced absorption (PA) under pumping conditions. As shown in Figs. S3, the two PA features exhibit diverse spectral and temporal dynamics. The high-energy PA peak (2.03 eV) shows an exponential decay feature with lifetime $\tau_d = 4.1$ ps, which can be attributed to the conversion from the initial hot carriers into A exciton, denoting photon scattering. While, the low energy PA peak (1.94 eV) shows an exponentially growing feature with lifetime τ_g =2.1 ps. Such a low energy PA feature is caused by the formation of trions excitons induced by pump-injected A excitons.[40] In comparison, two positive PB peaks at 1.85 eV and 2.00 eV correspond to A and B excitons of MoS_2, respectively. The results are biexponentially fitted. Note that the timescale of the electron–hole recombination of MoS_2 is longer than that of the WS_2 shell, indicating that the MoS_2 core with a weaker radiative recombination rate. Such a result is consistent with the PL experimental investigation in Fig. 3.

The TAM spectra acquired from the HS interface are shown in Fig. 4(c). Considering that the spot size (~ 4 μm) is close to the width of the depletion region, the MoS_2 core region and WS_2 shell region are both excited. The differential reflection signal intensity ($\Delta R/R_0$) is significantly reduced by $> 50\%$ compared with that of the core and shell, indicating the small exciton population at the interface. In the HS, the PB peak of MoS_2 is slightly blue-shifted, and that of WS_2 is somewhat red-shifted, compared with the corresponding peaks of isolated monolayers. Because there exist pairs of spatially separated electron and hole in the LHS, the energy shift is caused by the renormalization of band gap due to a very effective charge transfer. The temporal TA spectra (Fig. S5) also indicate that the excited electron–hole pairs can be separated immediately in MoS_2 and WS_2. These results are consistent with the density functional theory (DFT) simulations in Fig. S6, where a type-II band alignment of MoS_2/WS_2 LHS facilitates the effective charge separation. Interestingly, the electronic band structure shows almost no valence band offset. This valence band alignment will result in an ultrafast resonance hole transfer phenomenon, which is analog to the resonance electron transfer in the $WS_2/Cr_3Ge_2Te_6$ HSs.[42] The resonance hole transfer mechanism is illustrated schematically in Fig. 4(d). The energetic hole transfer from MoS_2 to WS_2 contributes to the trion recombination process, leading the PL quantum yield to further increase. Therefore, it can be easily found that the low-energy PA peak of the WS_2 trions in Fig. 4(c) disappears at the interface.

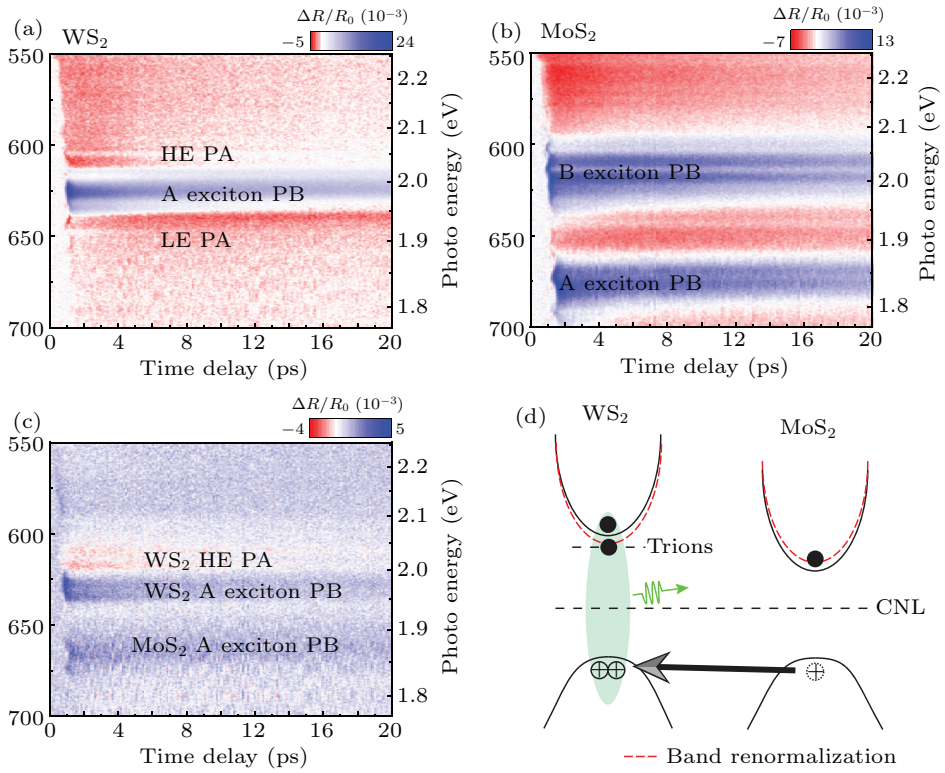


Fig. 4. ((a)–(c) Energy-resolved transient reflectance spectra of WS_2, MoS_2, and MoS_2/WS_2 LHS under being excited by 3.1-eV laser, showing exciton bleaching and absorption signals of WS_2 and MoS_2, respectively.

4. Conclusions

In this work, we conducted a spectrally-resolved and comprehensive analysis of anomalous PL enhancement in the vicinity of the interface of MoS_2/WS_2 LHSs. A red-shift of the enhanced PL energy indicates the proportion increase of the trion recombination in WS_2. The highly enhanced trion recombination can be ascribed to photoexcited carrier dynamics, which is facilitated by resonance hole transfer from MoS_2 side to WS_2 side. These findings provide further insights into the ultrafast carrier dynamics at the interface of the type-II 2D LHS.

Acknowledgements

Project supported by the National Natural Science Foundation of China (Grant No. 61804047), the Training Program for the Natural Science Foundation of Henan Normal University, China (Grant No. 2017PL02), the Scientific Research Start-up Foundation for PhD of Chaohu University, China (Grant No. KYQD-2023012), the Natural Science Foundation Henan Province of China (Grant No. 232300421236), and the High Performance Computing Center (HPCC) of Henan Normal University, China.

References

[1] Zhang Z, Ji X, Shi J, Zhou X, Zhang S, Hou Y, Qi Y, Fang Q, Ji Q, Zhang Y, Hong M, Yang P, Liu X, Zhang Q, Liao L, Jin C, Liu Z and Zhang Y 2017 *ACS Nano* **11** 4328

[2] Wang J, Yao Q, Huang C W, Zou X, Liao L, Chen S, Fan Z, Zhang K, Wu W, Xiao X, Jiang C and Wu W W 2016 *Adv. Mater.* **28** 8302

[3] Azizi A, Dogan M, Long H, Cain J D, Lee K, Eskandari R, Varieschi A, Glazer E C, Cohen M L and Zettl A 2020 *Nano Lett.* **20** 6120

[4] Sangwan V K, Lee H S, Bergeron H, Balla I, Beck M E, Chen K S and Hersam M C 2018 *Nature* **554** 500

[5] Wang Z, Rhodes D A, Watanabe K, Taniguchi T, Hone J C, Shan J and Mak K F 2019 *Nature* **574** 76

[6] Fei Z, Scott M E, Gosztola D J, Foley J J, Yan J, Mandrus D G, Wen H, Zhou P, Zhang D W, Sun Y, Guest J R, Gray S K, Bao W, Wiederrecht G P and Xu X 2016 *Phys. Rev. B* **94** 081402

[7] Paul K K, Kim J H and Lee Y H 2021 *Nat. Rev. Phys.* **3** 178

[8] Si M, Su C J, Jiang C, Conrad N J, Zhou H, Maize K D, Qiu G, Wu C T, Shakouri A, Alam M A and Ye P D 2018 *Nat. Nanotechnol.* **13** 24

[9] Rivera P, Schaibley J R, Jones A M, Ross J S, Wu S, Aivazian G, Klement P, Seyler K, Clark G, Ghimire N J, Yan J, Mandrus D G, Yao W and Xu X 2015 *Nat. Commun.* **6** 6242

[10] Gong Y, Lin J, Wang X, Shi G, Lei S, Lin Z, Zou X, Ye G, Vajtai R, Yakobson B I, Terrones H, Terrones M, Beng, Lou J, Pantelides S T, Liu Z, Zhou W and Ajayan P M 2014 *Nat. Mater.* **13** 1135

[11] Chiu M H, Zhang C, Shiu H W, Chuu C P, Chen C H, Chang C Y, Chen C H, Chou M Y, Shih C K and Li L J 2015 *Nat. Commun.* **6** 7666

[12] Hong X, Kim J, Shi S F, Zhang Y, Jin C, Sun Y, Tongay S, Wu J, Zhang Y and Wang F 2014 *Nat. Nanotechnol.* **9** 682

[13] Yuan J, Najmaei S, Zhang Z, Zhang J, Lei S, Ajayan P M, Yakobson B I and Lou J 2015 *ACS Nano* **9** 555

[14] Sun S, Dang J, Xie X, Yu Y, Yang L, Xiao S, Wu S, Peng K, Song F, Wang Y, Yang J, Qian C, Zuo Z and Xu X 2020 *Chin. Phys. Lett.* **37** 087801

[15] Zhao S, Tan J, Ke C, Feng S, Lai Y, Ding B, Luo G, Lin J and Liu B 2022 *Science China Materials* **65** 1034

[16] Ye K, Liu L, Liu Y, Nie A, Zhai K, Xiang J, Wang B, Wen F, Mu C, Zhao Z, Gong Y, Liu Z and Tian Y 2019 *Adv. Opt. Mater.* **7** 1900815

[17] Chen C, Yang Y, Zhou X, Xu W, Cui Q, Lu J, Jing H, Tian D, Xu C, Zhai T and Xu H 2021 *ACS Appl. Nano Mater.* **4** 5522

[18] Najafidehaghani E, Gan Z, George A, Lehnert T, Ngo G Q, Neumann C, Bucher T, Staude I, Kaiser D, Vogl T, Hübner U, Kaiser U, Eilenberger F and Turchanin A 2021 *Adv. Funct. Mater.* **31** 2101086

[19] Zhang Z, Chen P, Duan X, Zang K, Luo J and Duan X 2017 *Science* **357** 788

[20] Wang Z, Xie Y, Wang H, Wu R, Nan T, Zhan Y, Sun J, Jiang T, Zhao Y, Lei Y, Yang M, Wang W, Zhu Q, Ma X and Hao Y 2017 *Nanotechnology* **28** 325602

[21] Monkhorst H J and Pack J D 1976 *Phys. Rev. B* **13** 5188

[22] Blochl P E 1994 *Phys. Rev. B* **50** 17953

[23] Kresse G and Hafner J 1994 *Phys. Rev. B* **49** 14251

[24] Kresse G and Furthmüller J 1996 *Phys. Rev. B* **54** 11169

[25] Huang C, Wu S, Sanchez A M, Peters J J P, Beanland R, Ross J S, Rivera P, Yao W, Cobden D H and Xu X 2014 *Nat. Mater.* **13** 1096

[26] Li M Y, Shi Y, Cheng C C, Lu L S, Lin Y C, Tang H L, Tsai M L, Chu C W, Wei K H, He J H, Chang W H, Suenaga K and Li L J 2015 *Science* **349** 524

[27] Lee Y H, Zhang X Q, Zhang W, Chang M T, Lin C T, Chang K D, Yu Y C, Wang J T, Chang C S, Li L J and Lin T W 2012 *Adv. Mater.* **24** 2320

[28] Gutierrez H R, Perea-Lopez N, Elias A L, Berkdemir A, Wang B, Lv R, Lopez-Urias F, Crespi V H, Terrones H and Terrones M 2013 *Nano Lett.* **13** 3447

[29] Hu Z, Avila J, Wang X, Leong J F, Zhang Q, Liu Y, Asensio M C, Lu J, Carvalho A, Sow C H and Castro Neto A H 2019 *Nano Lett.* **19** 4641

[30] Chen K, Wan X, Xie W, Wen J, Kang Z, Zeng X, Chen H and Xu J 2015 *Adv. Mater.* **27** 6431

[31] Feng L P, Su J and Liu Z T 2014 *J. Alloys Compd.* **613** 122

[32] Han H V, Lu A Y, Lu L S, Huang J K, Li H, Hsu C L, Lin Y C, Chiu M H, Suenaga K, Chu C W, Kuo H C, Chang W H, Li L J and Shi Y 2016 *ACS Nano* **10** 1454

[33] McCreary A, Berkdemir A, Wang J, Nguyen M A, Elías A L, Perea-López N, Fujisawa K, Kabius B, Carozo V, Cullen D A, Mallouk T E, Zhu J and Terrones M 2016 *J. Mater. Res.* **31** 931

[34] Cong C, Shang J, Wang Y and Yu T 2018 *Adv. Opt. Mater.* **6** 1700767

[35] Sheng Y, Wang X, Fujisawa K, Ying S, Elias A L, Lin Z, Xu W, Zhou Y, Korsunsky A M, Bhaskaran H, Terrones M and Warner J H 2017 *ACS Appl. Mater. Interfaces* **9** 15005

[36] Guo Y and Robertson J 2016 *Appl. Phys. Lett.* **108** 233104

[37] Gaur A P S, Rivera A M, Dash S P, Dey S, Katiyar R S and Sahoo S 2019 *Appl. Phys. Lett.* **115** 173103

[38] Kim H, Yoon Y G, Ko H, Kim S M and Rho H 2019 *2D Mater.* **6** 025004

[39] Liu H, Wang C, Zuo Z, Liu D and Luo J 2020 *Adv. Mater.* **32** 1906540

[40] Vega-Mayoral V, Vella D, Borzda T, Prijatelj M, Tempra I, Pogna E A A, Dal Conte S, Topolovsek P, Vujicic N, Cerullo G, Mihailovic D and Gadermaier C 2016 *Nanoscale* **8** 5428

[41] Shi H, Yan R, Bertolazzi S, Brivio J, Gao B, Kis A, Jena D, Xing H G and Huang L 2013 *ACS Nano* **7** 1072

[42] Rahman S, Liu B, Wang B, Tang Y and Lu Y 2021 *ACS Appl. Mater. Interfaces* **13** 7423